nature nanotechnology

LETTERS

https://doi.org/10.1038/s41565-019-0504-0

Anomalous spin–orbit torques in magnetic single-layer films

Wenrui Wang[1,9], Tao Wang[2,9], Vivek P. Amin[3,4], Yang Wang[2], Anil Radhakrishnan[1], Angie Davidson[5], Shane R. Allen[5], T. J. Silva[6], Hendrik Ohldag[7], Davor Balzar[5], Barry L. Zink[5], Paul M. Haney[4], John Q. Xiao[2], David G. Cahill[8], Virginia O. Lorenz[1*] and Xin Fan[5*]

The spin Hall effect couples charge and spin transport[1–3], enabling electrical control of magnetization[4,5]. A quintessential example of spin-Hall-related transport is the anomalous Hall effect (AHE)[6], first observed in 1880, in which an electric current perpendicular to the magnetization in a magnetic film generates charge accumulation on the surfaces. Here, we report the observation of a counterpart of the AHE that we term the anomalous spin–orbit torque (ASOT), wherein an electric current parallel to the magnetization generates opposite spin–orbit torques on the surfaces of the magnetic film. We interpret the ASOT as being due to a spin-Hall-like current generated with an efficiency of 0.053 ± 0.003 in $Ni_{80}Fe_{20}$, comparable to the spin Hall angle of Pt[7]. Similar effects are also observed in other common ferromagnetic metals, including Co, Ni and Fe. First-principles calculations corroborate the order of magnitude of the measured values. This work suggests that a strong spin current with spin polarization transverse to the magnetization can be generated within a ferromagnet, despite spin dephasing[8]. The large magnitude of the ASOT should be taken into consideration when investigating spin–orbit torques in ferromagnetic/nonmagnetic bilayers.

The spin Hall effect can convert a charge current into a perpendicular flow of spin angular momentum, that is, a spin current[9]. One of its manifestations in a magnetic conductor is the anomalous Hall effect (AHE)[10], illustrated in Fig. 1a. Due to an imbalance of electrons with spins parallel and antiparallel to the magnetization, the flow of spin current results in charge accumulation on the top and bottom surfaces. The spin current in this configuration is polarized parallel to the magnetization[11–13]. Applying similar considerations to the configuration illustrated in Fig. 1b, in which the electric current is parallel to the magnetization, a spin current can also be generated, except with electron spins transverse to the magnetization. In single-layer ferromagnets with bulk inversion symmetry, the transversely polarized spin current does not give rise to a bulk spin–orbit torque (ferromagnets with broken bulk inversion symmetry have been shown to exhibit a non-zero bulk spin–orbit torque[14,15]). Instead, we predict that it will result in a net anomalous spin–orbit torque (ASOT) on the top and bottom surfaces, where inversion symmetry is broken (Supplementary Note 1). It should be noted that the term 'anomalous' here does not mean the ASOT has different behaviour from conventional spin–orbit torque[4] (the two have the same symmetry), but rather is used to illustrate its similarity to the AHE. Both ASOT and AHE are spin–orbit-interaction-induced phenomena that can be observed in single-layer magnetic conductors, under the different current and magnetization configurations illustrated in Fig. 1a,b.

Interconversion between transversely polarized spin current and charge current has been studied recently in ferromagnetic multilayers[16–19] with considerable spin–charge conversion efficiency. Due to strong spin dephasing[8,20], a transversely polarized spin current decays rapidly near the surface of the ferromagnet, so it is difficult to distinguish whether the spin–charge conversion observed in these studies is due to interfacial[21] or bulk spin–orbit interaction. Recently, it has been theoretically predicted that transversely polarized spin currents are allowed in diffusive ferromagnets[22]. In this Letter, we show that a transversely polarized spin current can also exist in ferromagnets in the clean limit. We refer to the mechanism of the current-induced transversely polarized spin current in the bulk ferromagnet as the transverse spin Hall effect (TSHE) (see Supplementary Fig. 2 for comparison with the longitudinal spin Hall effect in a ferromagnetic metal[11]).

Under the assumption that the current-induced ASOT in a ferromagnet results in a small perturbation to the magnetization, the ASOTs are equivalent to effective magnetic fields in the z direction[23] that tilt the magnetization out of plane, as illustrated in Fig. 1b. The out-of-plane magnetization tilting, m_z^{ASOT}, due to the ASOT at the top $\left(\tau_{\mathrm{T}}^{\mathrm{ASOT}}\right)$ and bottom $\left(\tau_{\mathrm{B}}^{\mathrm{ASOT}}\right)$ surfaces can be derived as

$$m_z^{\mathrm{ASOT}}(z) = \frac{\tau_{\mathrm{T}}^{\mathrm{ASOT}} \cosh\frac{d-z}{\lambda} + \tau_{\mathrm{B}}^{\mathrm{ASOT}} \cosh\frac{z}{\lambda}}{(|H_{\mathrm{ext}}| + M_{\mathrm{eff}})\mu_0 M_s \lambda \sinh\frac{d}{\lambda}} m_x \qquad (1)$$

where d is the total thickness of the film, λ is the exchange length, H_{ext} is an applied external magnetic field in the x direction, M_{eff} is the effective demagnetizing field, μ_0 is the vacuum permeability, M_s is the saturation magnetization and m_x is the projection of the unit magnetization along the x direction. Here, the ASOT is assumed to be located only at the surfaces, and the surface anisotropy is neglected. (See Supplementary Note 4 for the derivation of equation (1), a discussion of why ASOT can be treated as a pure surface effect, and a numerical analysis that takes into account the surface anisotropy.)

[1]Department of Physics, University of Illinois at Urbana-Champaign, Urbana, IL, USA. [2]Department of Physics and Astronomy, University of Delaware, Newark, DE, USA. [3]Maryland Nanocenter, University of Maryland, College Park, MD, USA. [4]Center for Nanoscale Science and Technology, National Institute of Standards and Technology, Gaithersburg, MD, USA. [5]Department of Physics and Astronomy, University of Denver, Denver, CO, USA. [6]Quantum Electromagnetics Division, National Institute of Standards and Technology, Boulder, CO, USA. [7]Stanford Synchrotron Radiation Lightsource, SLAC National Accelerator Laboratory, Menlo Park, CA, USA. [8]Department of Materials Science and Engineering, University of Illinois at Urbana-Champaign, Urbana, IL, USA. [9]These authors contributed equally: Wenrui Wang, Tao Wang. *e-mail: vlorenz@illinois.edu; xin.fan@du.edu

Because exchange coupling in the ferromagnet aligns the magnetization, the spatially antisymmetric magnetization tilting is expected to be measurable when the magnetic material is thicker than the exchange length (for example, 5.1 nm for $Ni_{80}Fe_{20}$). A simulation of the out-of-plane magnetization distribution due to ASOT in a 32 nm $Ni_{80}Fe_{20}$ (Py) film is shown in Fig. 1c.

To observe ASOT, we fabricated a sample with the following structure: substrate/AlO_x(2)/Py(32)/AlO_x(2)/SiO_2(3), where the numbers in parentheses are thicknesses in nanometres. The substrate is fused silica, which allows optical access to the bottom of the sample. Py is chosen because it is magnetically soft and widely used for the study of spin–orbit torques. The film is lithographically patterned into a 50 μm × 50 μm square and connected by gold contact pads, as shown in Fig. 2a. When an electric current I of 40 mA is applied directly through the sample, ASOTs at the top $\left(\tau_T^{ASOT}\right)$ and bottom $\left(\tau_B^{ASOT}\right)$ surfaces lead to non-uniform magnetization tilting, as described by equation (1). When a calibration current I_{cal} of 400 mA is passed around the sample, an out-of-plane Oersted field $\mu_0 h_{cal} \approx 0.85$ mT is generated that uniformly tilts the magnetization out of plane, which is used for calibrating the magnitude of the ASOTs:

$$m_z^{cal} = \frac{h_{cal}}{|H_{ext}| + M_{eff}} \quad (2)$$

We detect the magnetization changes using the polar magneto-optic Kerr effect (MOKE) by measuring the Kerr rotation θ_k and ellipticity change ε_k of the polarization of a linearly polarized laser reflected from the sample[24,25]. The penetration depth of the laser in Py is ~14 nm, which is less than half the thickness of the 32 nm Py. Therefore, the MOKE response is more sensitive to the ASOT-induced out-of-plane magnetization $m_z^{ASOT}(z)$ on the surface on which the laser is directly incident.

The Kerr rotation due to ASOT as a function of the external field (shown in Fig. 2c,d) resembles a magnetization hysteresis, as can be understood from equation (1). The overall offsets of the Kerr rotation signals are due to a residual, current-induced out-of-plane Oersted field due to imprecision in positioning the MOKE probe spot exactly at the centre of the sample (see Supplementary Fig. 5b for MOKE signal dependence on the laser spot position) and do not depend on the in-plane magnetization orientation[23]. In contrast, when a uniform calibration field h_{cal} is applied, the Kerr rotation is symmetric as a function of external field H_{ext} (Fig. 2e,f), consistent with equation (2). Our phenomenological model (Fig. 1c) predicts ASOT at the top and bottom surfaces to have the same magnitude but opposite directions, leading to opposite magnetization tilt at the two surfaces. Because we flip the sample to make the measurement of the bottom surface, the ASOT-induced Kerr rotation measured on the top (Fig. 2c) and bottom (Fig. 2d) surfaces are the same sign. In contrast, the Kerr rotation due to the calibration field (Fig. 2e,f) changes sign because h_{cal} is reversed on flipping the sample.

As shown in Fig. 3a, the MOKE response due to ASOT is linear with applied electric current, indicating no significant heating-related effects up to 5×10^{10} A m^{-2} current density. As shown in Fig. 3b, the polar MOKE response exhibits a cosine dependence on the relative angle between the electric current and the magnetization, consistent with equation (1).

To confirm that the ASOT depends on the current density, we grew a series of AlO_x(2)/Py(t)/AlO_x(2)/SiO_2(3) films on silicon substrates with 1-μm-thick thermal oxide, where t varied from 4 nm to 48 nm. For all samples, we apply the same current density of 5×10^{10} A m^{-2}, and use MOKE to quantify the ASOT. To fit the measured MOKE results, we use a propagation matrix method[24] (see Methods and Supplementary Note 5) to numerically simulate the MOKE signal as a function of the Py thickness. As presented in Fig. 3c, the validity of the method is first verified by a thickness-dependent calibration

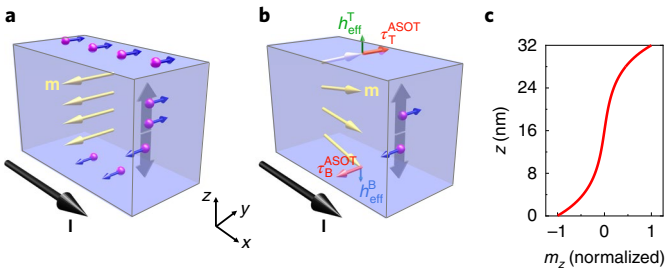

Fig. 1 | Illustrations of the AHE and ASOT. a, In the AHE, a charge current **I** (black arrow) perpendicular to the magnetization **m** (yellow arrows) generates a flow of spin current (grey arrows) in the z direction. Blue arrows on purple spheres represent spin directions of electrons. Due to the imbalance of majority and minority electrons, the flow of spin current results in spin and charge accumulation on the top and bottom surfaces. **b**, When a charge current is applied parallel to the magnetization, the AHE vanishes, but spin–orbit interaction generates a flow of transversely polarized spin current that gives rise to ASOT. Under the assumption that the current-induced ASOT in a ferromagnet results in a small perturbation to the magnetization, ASOTs (red arrows) are equivalent to out-of-plane fields (green arrows) that tilt the magnetization out of plane. $\tau_T^{ASOT}\left(\tau_B^{ASOT}\right)$ and $h_{eff}^T\left(h_{eff}^B\right)$ are the ASOTs and equivalent fields at the top (bottom) surfaces, respectively. **c**, Simulated distribution of the out-of-plane magnetization m_z in a 32 nm Py film driven by equal and opposite ASOTs on the surfaces, scaled by the maximum value.

measurements, where a uniform 0.85 mT out-of-plane calibration field is applied to all samples. To extract the ASOT amplitude, the top-surface Kerr rotation and the ellipticity change due to the ASOT is fitted in Fig. 3d. The only free fitting parameter is the ASOT on the top surface, τ_T^{ASOT}, which is assumed to be the same for all Py thicknesses under the same current density and to have equal magnitude and opposite sign as the ASOT on the bottom surface τ_B^{ASOT}. The good agreement between experiment and simulation confirms that the ASOTs depend on current density. The ASOTs are extrapolated to be $\tau_T^{ASOT} = \tau_B^{ASOT} = (-0.86 \pm 0.04) \times 10^{-6}$ J m^{-2} from the fitting. Relating this torque to a spin current allows us to find the spin-Hall-angle-like efficiency of the ASOT, $\xi = \frac{2e\tau_B^{ASOT}}{j_e \hbar} = 0.053 \pm 0.003$, where e is the electron charge, j_e is the electric current density and $\hbar$ is the reduced Planck constant; this efficiency is comparable to the effective spin Hall angle of Pt (0.056 ± 0.005) measured in a Pt/Py bilayer[7]. The corresponding ASOT conductivity for 32 nm Py is calculated as $\sigma^{ASOT} = \frac{2e}{\hbar}\frac{\tau_B^{ASOT}}{E} = \xi\sigma = 2,300 \pm 120\ \Omega^{-1}$ cm^{-1}, where E is the applied electric field. In Fig. 3d, the deviation of the ASOT-induced Kerr ellipticity from the model for the 4 nm Py sample can be accounted for if a 1% variation between τ_T^{ASOT} and τ_B^{ASOT} is assumed, which may be due to a slight difference in spin relaxation at the two interfaces (Supplementary Note 6).

Given that ASOT results in magnetization changes near the surface, the extracted ASOT values may be influenced by spin–orbit interaction at the interface with the capping layer[19,26,27]. To determine the relative contribution of such interface effects, we compare the ASOT at the top surface of the AlO_x(3)/Py(32)/AlO_x(3) sample with the total spin–orbit torque (SOT) in a series of control samples, AlO_x(3)/Py(4)/Cap, where Cap is varied among AlO_x(3), AlO_y(3, different oxidation time), SiO_2(3), Cu(3)/SiO_2(3) and Al(3)/SiO_2(3). These capping layer materials are often assumed to have weak spin–orbit interaction because they are light elements, but they will change the electrostatic properties and band structure of the top interface. The bottom surface is the same as for the 32 nm Py sample. Because Py is only 4 nm in these control samples (thinner than the exchange length), the magnetization uniformly responds

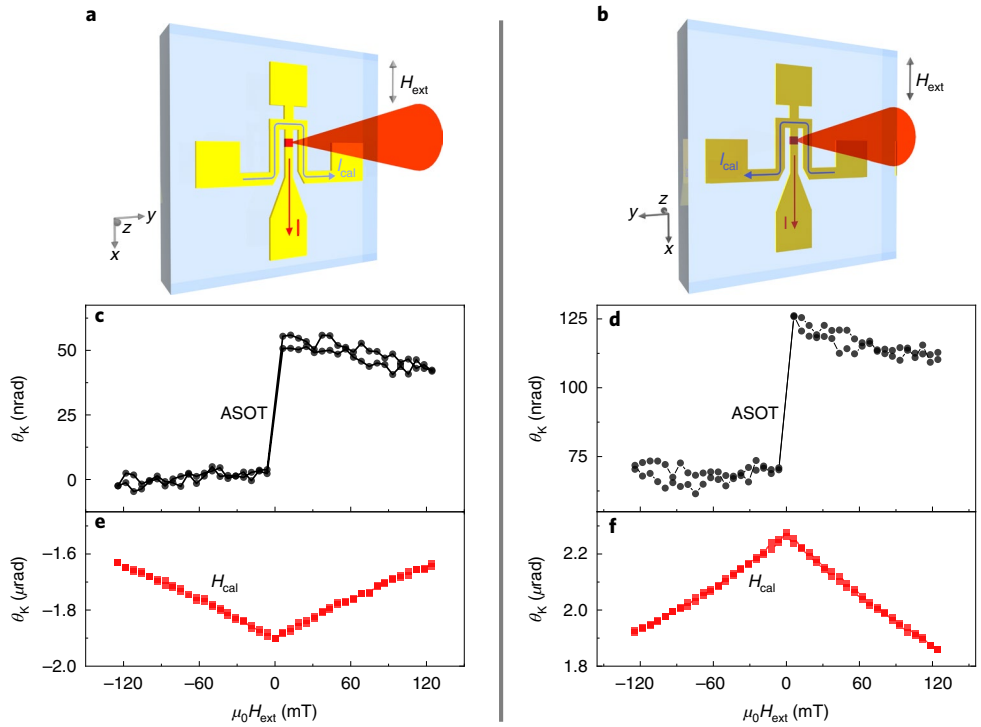

Fig. 2 | Symmetry of the ASOT. a,**b**, Diagrams of the measurement configurations with the laser incident on the top (**a**) and bottom (**b**) of the sample. The red square is the sample with a size of 50 μm × 50 μm and yellow pads are gold contacts. The plots below each diagram correspond to signals measured in that diagram's configuration. **c**,**d**, Measured Kerr rotation signals for when current is applied through the sample, which arise from ASOTs. **e**,**f**, Measured Kerr rotation signals for when the calibration field h_{Cal} is applied.

Table 1 | Measured and calculated electrical, AHE and ASOT conductivities

		Ni	Fe	Co
Calculation	Structure	fcc	bcc	hcp
	AHE conductivity	−1.3	0.72	0.45
	TSHE conductivity	3.92	1.05	−0.24
Experiment	Structure	fcc	bcc	hcp
	Conductivity	56	32	46
	AHE conductivity	−0.5 ± 0.05	0.5 ± 0.05	0.3 ± 0.03
	ASOT conductivity	3.5 ± 0.1	−1.0 ± 0.2	0.8 ± 0.5

All values have units of $10^3 \Omega^{-1}$ cm^{-1}. All experimental data are extrapolated based on 40 nm sputtered polycrystalline films, sandwiched between two 3 nm AlO_x layers. Additional materials parameters are provided in Supplementary Table 1 and Supplementary Fig. 3. The positive sign for the ASOT conductivity corresponds to the scenario that if the applied electric field is in the *x* direction, the generated spin current flowing in the *z* direction has spin moment in the *y* direction. Under this choice, the spin Hall conductivity of Pt is positive. fcc, face-centred cubic; bcc, body-centred cubic; hcp, hexagonal close-packed.

to the total SOT, which is a sum of the ASOTs at the top and bottom surfaces $\left(\tau_T^{ASOT} + \tau_B^{ASOT}\right)$. Interfacial spin–orbit effects, like the Rashba–Edelstein effect or interface-generated spin currents, are highly material- and structure-specific[21,28]. For this reason, if either effect played an important role in the ASOT, we would not expect quantitatively, or even qualitatively, similar results for interfaces with substantially different characteristics (Supplementary Note 7). Should there be a significant interface-dependence of the ASOT, a large total SOT will be observed in some of these control samples with asymmetric interfaces. As shown in Fig. 3e, all samples exhibit total SOT conductivities $\sigma_{tot}^{SOT} = \frac{2e}{\hbar}\left(\tau_T^{ASOT} + \tau_B^{ASOT}\right)/E$ of at most 4% of the bottom-surface ASOT conductivity of the 32 nm Py sample. This suggests that the top-surface ASOT, which varies less than 4% among Py with different capping layers, does not contain a substantial contribution from the interface of the Py with the capping layers.

The insensitivity of ASOT to the interface implies that it arises from the bulk spin–orbit interaction within the magnetic material. One possible mechanism is the TSHE illustrated in Fig. 1b. We evaluate the TSHE conductivity using the linear response in the Kubo formalism in the clean limit using density functional theory (DFT)[29,30](see Supplementary Note 8 for technical details). First-principles calculations for Ni, Fe and Co all show significant TSHE conductivities, as summarized in Table 1. We also measure the ASOT conductivities of these materials experimentally (provided in Table 1). For comparison, we calculate and measure the AHE conductivities for these materials. If the ASOT is only due to the TSHE from the intrinsic band structure, the calculated TSHE conductivity should match the measured ASOT conductivity. As shown in Table 1, the conductivities are similar in magnitude as those calculated, indicating that the intrinsic mechanism may significantly contribute to

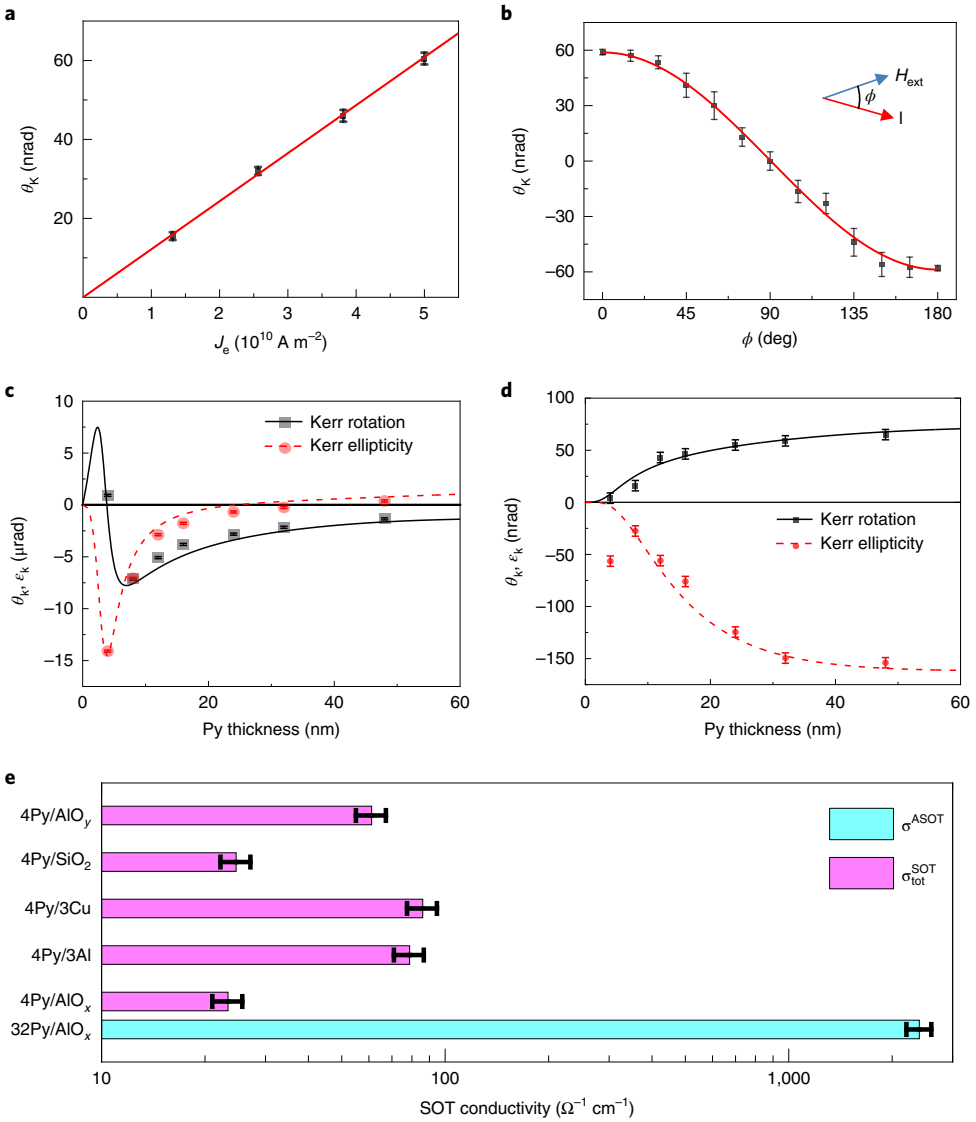

Fig. 3 | Dependence of ASOT on current density, angle, thickness and the interface. a,**b**, Kerr rotation change as a function of current density (**a**) and the angle between current direction and magnetization (**b**). **c**,**d**, Kerr rotation (experimental, black squares; fit, black solid line) and ellipticity change (experimental, red circles; fit, red dashed line) due to the calibration field (**c**) and due to ASOT (**d**). **e**, Comparison between total SOT conductivities σ^{SOT}_{tot} measured for 4 nm Py with different capping layers, and the bottom-surface ASOT conductivity σ^{ASOT} of 32 nm Py. Error bars indicate single s.d. uncertainties, obtained from linear extrapolation of ASOT-induced MOKE data at positive/negative magnetic fields, as explained in the Methods. In all these samples, the other side of the Py is in contact with AlO_x.

the ASOT. However, the signs for Fe and Co are opposite between measured and calculated values; this may be because the intrinsic mechanism is not the sole source of ASOT and other mechanisms should be taken into account. By analogy with the AHE, we expect that extrinsic mechanisms such as skew scattering[10,31] can also contribute to generating transversely polarized spin current and hence ASOT (Supplementary Fig. 10).

The existence of ASOT may change the conventional understanding of spin–orbit torques in magnetic multilayers. As an example, we study a SiO_2/Py/Cu/Pt multilayer; here, an electric current can generate a net spin–orbit torque acting on the Py magnetization. The net spin–orbit torque is the superposition of spin–orbit torques at the two surfaces of the Py layer. Although the Pt or the Pt/Cu interface is often thought to be the source of spin–orbit torque in such systems, we find experimentally that the spin–orbit torque at the SiO_2/Py interface is much larger than that at the Py/Cu interface, as shown in Fig. 4. This is because the spin–orbit torque at the Py/Cu interface is a superposition of ASOT in the Py and the external spin–orbit torque due to spin current generated from the Pt, the two of which are in opposite directions. Therefore, although the total spin–orbit torque appears to be consistent with the spin Hall angle of Pt, the actual spin–orbit torque at the SiO_2/Py interface is in fact greater than that at the Py/Cu interface.

Although the total ASOT equals zero in an isolated magnetic layer with symmetric surfaces, such symmetry is probably broken when a ferromagnet is in contact with a non-magnetic layer with strong spin–orbit coupling (Supplementary Note 10). If there is an asymmetry in the ASOT at the two surfaces of the magnetic layer, a net spin–orbit torque is expected, which contributes to the total spin–orbit torque in magnetic multilayers. This net spin–orbit torque, arising from the spin–orbit interaction of the ferromagnet itself, may have been overlooked previously.

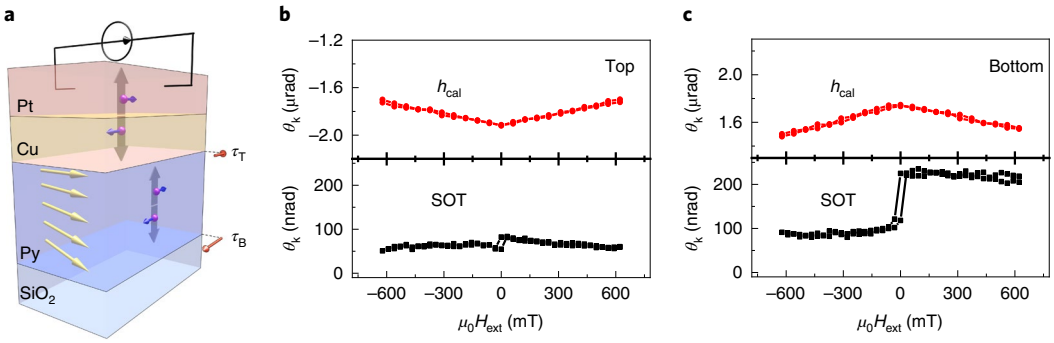

Fig. 4 | Anomalous spin–orbit torque modifies the net current-induced surface spin torques in a Py/Cu/Pt multilayer. a, Illustration of the asymmetric SOTs in a SiO_2/Py(32)/Cu(3)/Pt(2)/AlO_x(3) multilayer. Grey arrows, spin current directions; blue arrows on purple spheres, spin directions; yellow arrows, magnetizations; red arrows, spin torque directions. Measurement configurations are the same as in Fig. 2. Net spin torques at the top surface $\tau_T = \tau_T^{ASOT} + \tau_{Pt/Cu}$ and at the bottom surface $\tau_B = \tau_B^{ASOT}$ are probed by MOKE, where $\tau_{Pt/Cu}$ is the spin–orbit torque due to spin current generated from Pt injected into Py. From the indicated spin currents, it can be expected that τ_T is smaller than τ_B, contrary to common understanding. **b**, Measured Kerr rotation signals when light probes the top surface with calibration field h_{cal} applied (top plot) and current-driven spin–orbit torque applied (bottom plot). **c**, Measured Kerr rotation signals when the bottom surface is interrogated with calibration field h_{cal} applied (top plot) and current-driven spin–orbit torque applied (bottom plot). Although the Kerr rotations due to the calibration signal are similar in magnitude, those due to current-driven spin–orbit torque are much larger at the bottom surface than at the top surface.

Online content

Any methods, additional references, Nature Research reporting summaries, source data, statements of code and data availability and associated accession codes are available at https://doi.org/10.1038/s41565-019-0504-0.

Received: 12 March 2019; Accepted: 13 June 2019;
Published online: 22 July 2019

References

1. Hirsch, J. E. Spin Hall effect. *Phys. Rev. Lett.* **83**, 1834–1837 (1999).
2. Kato, Y. K., Myers, R. C., Gossard, A. C. & Awschalom, D. D. Observation of the spin Hall effect in semiconductors. *Science* **306**, 1910–1913 (2004).
3. Kimura, T., Otani, Y., Sato, T., Takahashi, S. & Maekawa, S. Room-temperature reversible spin Hall effect. *Phys. Rev. Lett.* **98**, 156601 (2007).
4. Liu, L. et al. Spin–torque switching with the giant spin Hall effect of tantalum. *Science* **336**, 555–558 (2012).
5. Emori, S., Bauer, U., Ahn, S.-M., Martinez, E. & Beach, G. S. D. Current-driven dynamics of chiral ferromagnetic domain walls. *Nat. Mater.* **12**, 611–616 (2013).
6. Hall, E. H. On the 'rotational coefficient' in nickel and cobalt. *Proc. Phys. Soc. Lond.* **4**, 325 (1880).
7. Liu, L., Moriyama, T., Ralph, D. C. & Buhrman, R. A. Spin–torque ferromagnetic resonance induced by the spin Hall effect. *Phys. Rev. Lett.* **106**, 036601 (2011).
8. Ghosh, A., Auffret, S., Ebels, U. & Bailey, W. E. Penetration depth of transverse spin current in ultrathin ferromagnets. *Phys. Rev. Lett.* **109**, 127202 (2012).
9. Zhang, S. F. Spin Hall effect in the presence of spin diffusion. *Phys. Rev. Lett.* **85**, 393–396 (2000).
10. Nagaosa, N., Sinova, J., Onoda, S., MacDonald, A. H. & Ong, N. P. Anomalous Hall effect. *Rev. Mod. Phys.* **82**, 1539–1592 (2010).
11. Miao, B. F., Huang, S. Y., Qu, D. & Chien, C. L. Inverse spin Hall effect in a ferromagnetic metal. *Phys. Rev. Lett.* **111**, 066602 (2013).
12. Taniguchi, T., Grollier, J. & Stiles, M. D. Spin–transfer torques generated by the anomalous Hall effect and anisotropic magnetoresistance. *Phys. Rev. Appl.* **3**, 044001 (2015).
13. Wang, H. L., Du, C. H., Hammel, P. C. & Yang, F. Y. Spin current and inverse spin Hall effect in ferromagnetic metals probed by $Y_3Fe_5O_{12}$-based spin pumping. *Appl. Phys. Lett.* **104**, 202405 (2014).
14. Chernyshov, A. et al. Evidence for reversible control of magnetization in a ferromagnetic material by means of spin–orbit magnetic field. *Nat. Phys.* **5**, 656–659 (2009).
15. Ciccarelli, C. et al. Room-temperature spin–orbit torque in NiMnSb. *Nat. Phys.* **12**, 855–860 (2016).
16. Tian, D. et al. Manipulation of pure spin current in ferromagnetic metals independent of magnetization. *Phys. Rev. B* **94**, 020403 (2016).
17. Das, K. S., Schoemaker, W. Y., van Wees, B. J. & Vera-Marun, I. J. Spin injection and detection via the anomalous spin Hall effect of a ferromagnetic metal. *Phys. Rev. B* **96**, 220408 (2017).
18. Humphries, A. M. et al. Observation of spin–orbit effects with spin rotation symmetry. *Nat. Commun.* **8**, 911 (2017).
19. Baek, S. H. C. et al. Spin currents and spin–orbit torques in ferromagnetic trilayers. *Nat. Mater.* **17**, 509–513 (2018).
20. Ralph, D. C. & Stiles, M. D. Spin transfer torques. *J. Magn. Magn. Mater.* **320**, 1190–1216 (2008).
21. Amin, V. P., Zemen, J. & Stiles, M. D. Interface-generated spin currents. *Phys. Rev. Lett.* **121**, 136805 (2018).
22. Pauyac, C. O., Chshiev, M., Manchon, A. & Nikolaev, S. A. Spin Hall and spin swapping torques in diffusive ferromagnets. *Phys. Rev. Lett.* **120**, 176802 (2018).
23. Fan, X. et al. Quantifying interface and bulk contributions to spin–orbit torque in magnetic bilayers. *Nat. Commun.* **5**, 3042 (2014).
24. Qiu, Z. Q. & Bader, S. D. Surface magneto-optic Kerr effect. *Rev. Sci. Instrum.* **71**, 1243–1255 (2000).
25. Fan, X. et al. All-optical vector measurement of spin–orbit-induced torques using both polar and quadratic magneto-optic Kerr effects. *Appl. Phys. Lett.* **109**, 122406 (2016).
26. Pesin, D. A. & MacDonald, A. H. Quantum kinetic theory of current-induced torques in Rashba ferromagnets. *Phys. Rev. B* **86**, 014416 (2012).
27. Kurebayashi, H. et al. An antidamping spin–orbit torque originating from the Berry curvature. *Nat. Nanotechnol.* **9**, 211–217 (2014).
28. Park, S. R., Kim, C. H., Yu, J., Han, J. H. & Kim, C. Orbital-angular-momentum based origin of Rashba-type surface band splitting. *Phys. Rev. Lett.* **107**, 156803 (2011).
29. Wang, X. J., Yates, J. R., Souza, I. & Vanderbilt, D. Ab initio calculation of the anomalous Hall conductivity by Wannier interpolation. *Phys. Rev. B* **74**, 195118 (2006).
30. Amin, V. P., Li, J., Stiles, M. D. & Haney, P. M. Intrinsic spin currents in ferromagnets.*Phys. Rev. B* **99**, 220405(R) (2019).
31. Hoffmann, A. Spin Hall effects in metals. *IEEE Trans. Magn.* **49**, 5172–5193 (2013).

Acknowledgements

The work carried out at the University of Denver is partially supported by the PROF and by the National Science Foundation under grant no. ECCS-1738679. W.W., D.G.C. and V.O.L. acknowledge support from the NSF-MRSEC under award no. DMR-1720633. T.W., Y.W. and J.Q.X. acknowledge support from the NSF under award no. DMR-1505192. V.P.A. acknowledges support under the Cooperative Research Agreement between the University of Maryland and the National Institute of Standards and Technology Center for Nanoscale Science and Technology, award 70NANB14H209, through the University of Maryland. The authors also thank M. Stiles and E. Jue for critical reading of the manuscript and X. Li for illuminating discussions.

Author contributions

X.F. and H.O. conceived the idea and X.F., W.W. and T.W. designed the experiments. T.W. fabricated the sample. T.W., Y.W., W.W., A.R., A.D., T.J.S., D.B. and B.L.Z. patterned and characterized the samples. W.W. performed the MOKE measurements and W.W., X.F., V.O.L., D.G.C. and J.Q.X. analysed the data. V.P.A. and P.M.H. carried out the first-principles calculations. X.F., W.W., V.O.L., V.P.A. and P.M.H. prepared the manuscript. All authors commented on the manuscript.

Competing interests

The authors declare no competing interests.

Additional information

Supplementary information is available for this paper at https://doi.org/10.1038/s41565-019-0504-0.

Correspondence and requests for materials should be addressed to V.O.L. or X.F.

Peer review information: *Nature Nanotechnology* thanks Chi-Feng Pai and other, anonymous, reviewer(s) for their contribution to the peer review of this work.

Methods

Sample fabrication. The samples used in this study were fabricated by magnetron sputtering. The AlO_x layers were made by depositing 2 nm Al film and subsequent oxidization in an oxygen plasma.

MOKE measurement of ASOT. The MOKE measurements were performed with a lock-in balanced detection system[25], as illustrated in Supplementary Fig. 4. An alternating current with frequency 20.15 kHz was applied through the patterned sample and the ASOT-induced MOKE response at the same frequency was measured. We used a Ti:sapphire mode-locked laser with ~100 fs pulses at a repetition rate of 80 MHz with a centre wavelength of 780 nm; the detectors used are slow relative to the repetition rate, so the measured signals were averaged over the pulses. The laser beam was focused by a ×10 microscope objective into a spot of ~4 μm diameter. Laser power below 4 mW was used to avoid significant heating effects. To eliminate the quadratic MOKE contribution, the average was taken of the signals for incident laser polarizations of 45° and 135° with respect to the magnetization[25]. A combination of a second half-wave plate and a Wollaston prism was used to analyse the Kerr rotation signal. For Kerr ellipticity measurements, a quarter-wave plate was inserted before the half-wave plate. We separated the MOKE data measured at positively and negatively saturated fields, and carried out linear extrapolation on the data. Half the difference in the extrapolated y-axis intercepts was taken as the MOKE signal corresponding to the ASOT. The error in the ASOT-induced MOKE signal was calculated by propagation of uncertainties, which are the standard deviations of the intercepts from the linear extrapolations of data at positively and negatively saturated fields.

Fitting of the thickness-dependent MOKE signal. In the simulations, the magnetic film was discretized into many sublayers of thickness 0.4 nm. By assuming equal and opposite ASOT, $\tau_T^{ASOT} = -\tau_B^{ASOT}$, at the very top and very bottom sublayers, respectively, we calculated the resultant out-of-plane magnetization using numerical methods (Supplementary Note 4). For calibration, a constant out-of-plane calibration field h_{cal} was applied to all sublayers, and the out-of-plane magnetization was calculated using the same numerical methods. Based on the calculated out-of-plane magnetization distribution, the polar MOKE response was determined using the propagation matrix method and taking into account multiple reflections (Supplementary Note 5). The above processes provide linear relationships between τ_T^{ASOT} and h_{cal} with the predicted MOKE response for various film thicknesses. In modelling the thickness-dependent MOKE response for calibration, shown in Fig. 3c, all parameters were measured by other techniques. The good agreement corroborates our numerical model. In the fitting of the thickness-dependent MOKE response due to ASOT, shown in Fig. 3d, we assumed that fitting parameter τ_T^{ASOT} was the same for all film thicknesses under the same current density. All other parameters were the same as those used in modelling the calibration result. The good agreement shown in Fig. 3d confirms our assumption that τ_T^{ASOT} depends on the current density. All the uncertainties in this Letter are single s.d. uncertainties. The principle source of uncertainty in the analysis is the fitting uncertainty, which was determined by a linear regression analysis by plotting the experimental data as a function of the simulation results.

Data availability

The MOKE measurement data are available at the Illinois Data Bank at https://doi.org/10.13012/B2IDB-7281207_V1. The data that support the plots within this paper and other findings of this study are available from the corresponding authors upon reasonable request.

Code availability

The code to numerically simulate the MOKE response using the propagation matrix method is available at the Illinois Data Bank at https://doi.org/10.13012/B2IDB-7281207_V1.